



UNIVERSITY OF LEEDS

This is a repository copy of *Investigation of the tribological and mechanical properties of FeCrMoCB coating on AISI 52100 Bearing steel*.

White Rose Research Online URL for this paper:

<https://eprints.whiterose.ac.uk/220006/>

Version: Accepted Version

---

**Article:**

Saharudin, M.F., Zulkifli, N.W.M., Goh, Y. et al. (3 more authors) (2025) Investigation of the tribological and mechanical properties of FeCrMoCB coating on AISI 52100 Bearing steel. *Tribology International*, 203. 110401. ISSN 0301-679X

<https://doi.org/10.1016/j.triboint.2024.110401>

---

This is an author produced version of an article published in *Tribology International*, made available under the terms of the Creative Commons Attribution License (CC-BY), which permits unrestricted use, distribution and reproduction in any medium, provided the original work is properly cited.

**Reuse**

This article is distributed under the terms of the Creative Commons Attribution (CC BY) licence. This licence allows you to distribute, remix, tweak, and build upon the work, even commercially, as long as you credit the authors for the original work. More information and the full terms of the licence here:

<https://creativecommons.org/licenses/>

**Takedown**

If you consider content in White Rose Research Online to be in breach of UK law, please notify us by emailing [eprints@whiterose.ac.uk](mailto:eprints@whiterose.ac.uk) including the URL of the record and the reason for the withdrawal request.



[eprints@whiterose.ac.uk](mailto:eprints@whiterose.ac.uk)  
<https://eprints.whiterose.ac.uk/>

# Investigation of the tribological and mechanical properties of FeCrMoCB coating on AISI 52100 Bearing steel

M.F. Saharudin<sup>1,2,\*</sup>, N.W.M. Zulkifli<sup>1,2,\*</sup>, Y. Goh<sup>2</sup>, Mahmoud Z. Ibrahim<sup>2,3,4,\*\*\*</sup>, A. Morina<sup>5</sup>,  
R.Mehtab<sup>1,2</sup>

<sup>1</sup>Centre for Energy Sciences, Department of Mechanical Engineering, Faculty of Engineering,  
University of Malaya, 50603 Kuala Lumpur, Malaysia.

<sup>2</sup>Department of Mechanical Engineering, Faculty of Engineering, University of Malaya,  
50603 Kuala Lumpur, Malaysia

<sup>3</sup> Advanced Manufacturing and Materials Processing Centre (AMMP), Faculty of Engineering, University of Malaya, 50603  
Kuala Lumpur, Malaysia

<sup>4</sup> Department of Design and Production Engineering, Faculty of Engineering, Ain Shams University, Cairo 11517, Egypt

<sup>5</sup> University of Leeds, School of Mechanical Engineering, Institute of Functional Surfaces, Leeds, UK

Corresponding author [nurinmz@um.edu.my](mailto:nurinmz@um.edu.my)\*; [firdausaharudin@gmail.com](mailto:firdausaharudin@gmail.com)\*\*; [mahmoudzakaria@um.edu.my](mailto:mahmoudzakaria@um.edu.my)\*\*\*

## Abstract

This study examines the mechanical and tribological properties of FeCrMoCB amorphous coatings on AISI 52100 bearing steel using laser cladding (LC). Two samples with varying LC parameters were compared to uncoated polished steel. Analytical methods included scanning electron microscopy (SEM), X-ray diffraction (XRD), microhardness testing and tribological tests via a high-frequency reciprocating rig (HFRR) tribometer under both dry and lubricated conditions, were employed. Sample S1 exhibited a microhardness five times that of uncoated steel and a 95% reduction in wear volume loss under dry conditions. Under grease-lubricated, S1 showed a 20% reduction in the coefficient of friction and a 93% reduction in wear volume loss. Sample S2 also outperformed uncoated steel. These results highlight the significant benefits of FeCrMoCB coatings.

**Keywords:** AISI 52100 steel, Fe-based amorphous coating, amorphous content, Laser cladding, wear resistance, microhardness, tribological properties.

## 26 **1 Introduction**

27 Wear is the gradual, unwanted loss pertaining to material from mechanical components' surfaces. The  
28 tribological qualities of these components are successfully enhanced by surface engineering technology, which applies  
29 high-performance coatings to their surfaces to reduce deterioration. Amorphous and nanocrystalline materials, as  
30 promising new materials, are becoming more and more popular in a number of industries because of their improved  
31 mechanical qualities, which include strength, wear resistance, hardness, as well as corrosion resistance [1], [2]. Fe-  
32 based amorphous alloys are widely acknowledged for their exceptional mechanical, magnetic, corrosion, and wear  
33 resistance properties [3], [4]. Still, their use is limited to powders, thin strips, and millimeter rods due to production  
34 challenges and brittleness [5] To overcome the application limitations of Fe-based amorphous alloys, they are  
35 fabricated into coatings, addressing room temperature brittleness and size constraints while retaining their inherent  
36 properties. Surface coating technology effectively expands the functions of Fe-based amorphous alloys in  
37 engineering by depositing a thin coating onto a substrate, thereby utilizing the alloy's properties and reducing material  
38 costs [6]. The preparation of crack-free metallic amorphous coatings is challenging due to the thermal stress induced  
39 during the laser-cladding process and the intrinsic brittleness of metallic glasses [7].

40 Various techniques are employed to prepare crack-free Fe-based amorphous coatings, which include plasma  
41 spray, high-velocity oxygen fuel (HVOF), arc spray, laser cladding (LC) detonation spray, as well as many others.  
42 Nevertheless, as the powder particles are sprayed in a semi-molten condition, they get plastically distorted and piled  
43 on the substrate, which results in an amorphous coating with high porosity (2% to 5%) as well as low adhesion strength.  
44 In comparison to other preparation techniques, LC offers several advantages, including rapid cooling rates (up to 10<sup>11</sup>  
45 K/s), metallurgical bonding, simplicity in automation, low heat-affected zones, as well as no pollution [8]. Amorphous  
46 coatings fabricated via LC technology exhibit notable benefits, such as minimized crack formation, low dilution rates,  
47 precise size regulation, and straightforward scalability for industrial production [9]. Hence, employing laser  
48 technology for amorphous coating preparation represents a novel surface processing approach that harnesses the rapid  
49 heating and cooling properties of lasers, along with the respective advantages of amorphous alloys [10].

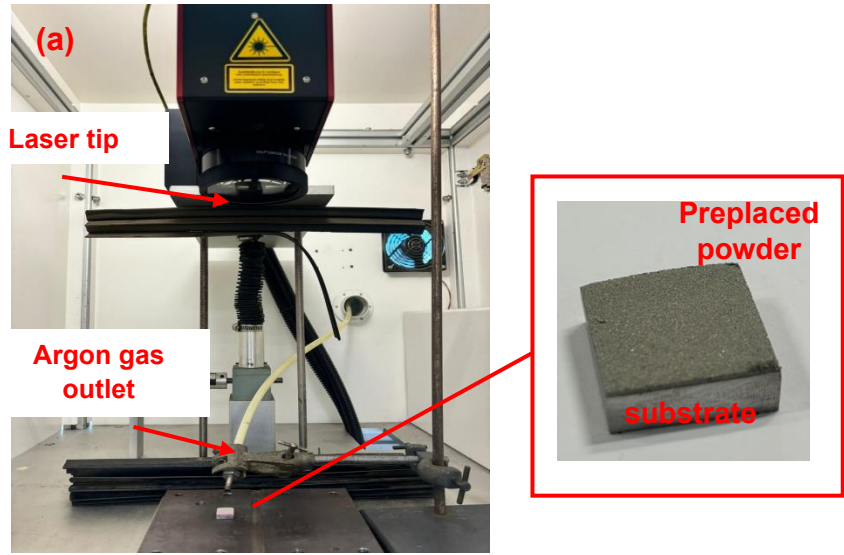
50 In recent decades, researchers have extensively explored LC utilization to prepare Fe-based amorphous coatings.  
51 Research has concentrated on the effects of scanning speed, laser power, powder feeding rate, as well as additional  
52 factors on the mechanical and microstructure characteristics of the resultant coatings [11]. To further demonstrate, S.

53 L. Wang [12] created Fe-based amorphous composite coatings with a composition of  
54  $\text{Fe}_{44.72}\text{Co}_{8.57}\text{Cr}_{14.95}\text{Mo}_{26.9}\text{C}_{3.2}\text{B}_{1.28}\text{Y}_{3.01}$  (wt.%) by LC on mild steel surfaces. These coatings outperformed 316L  
55 stainless steel in NaCl solution in terms of wear and corrosion resistance because they had fewer pores as well as  
56 cracks and were metallurgically attributed to the substrate. Major elements (Ni, Co, Fe, Cr), small atom elements (B,  
57 Si, C, P), as well as large atom elements (Y, W, Zr Mo, Nb) (MSL), are currently found in the more advanced Fe-based  
58 amorphous systems [13]. Performance-wise, wear resistance as well as mechanical characteristics are the main areas  
59 of study for Fe-based amorphous coatings, usually with a constant composition [14].

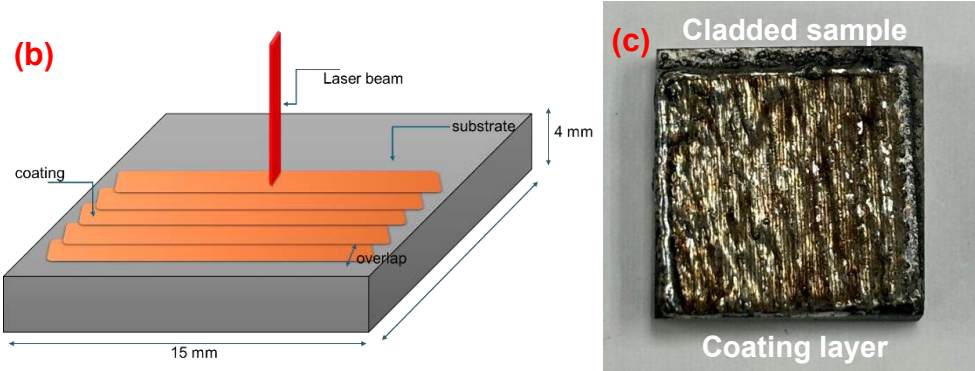
60 Enhancing the tribological performance of AISI 52100 steel is the goal of surface coating. The idea of creating  
61 a novel FeCrMoCB amorphous-crystalline composite coating layer that offers longer-term mechanical qualities and  
62 increased wear resistance is being investigated, which is unique. The macroscopic shape, microstructure, as well as  
63 performance of the cladding layer are influenced by several process parameters, each of which also impacts the others.  
64 In practical applications, it is essential to comprehensively consider various process parameters based on the specific  
65 requirements of the cladding layer. Hence, the present research fills the gap by offering the first evaluation of AISI  
66 52100 steel's grease-lubricated wear resistance.

## 67 **2 Materials and experimental procedures**

68 The substrate material was AISI 52100 steel substrates measuring  $15 \times 15 \times 4$  mm. As per the earlier research  
69 [15], the substrates were polished utilizing 240-grit SiC sandpaper washed in an ultrasonic bath with deionized water  
70 as well as acetone, followed by drying at room temperature. FeCrMoCB amorphous powder (0.75g) from LiquidMetal  
71 Coatings® with a nominal particle size range of 20–80  $\mu\text{m}$  as the coating material was preplaced on each substrate  
72 using custom mold, evenly distributed with acetone, dried with a hairdryer under room temperature, and formed a  
73 layer approximately 430  $\mu\text{m}$  thick before coating deposition. Using a fiber laser device (ROFIN StarFiber 300,  
74 Germany), the samples were created with a peak power of 300 W and operated at a wavelength of  $1070 \pm 10$  nm. The  
75 LC setup is shown in Figures 1(a), (b), and (c), which includes preplaced powder on the substrate, laser scanning  
76 direction, overlap designations, and sample images before and after cladding.



77



78

79 **Figure 1:** (a) LC configuration, (b) laser scanning orientation and (c) visual representation of the sample post-  
80 LC

81 The study involved the LC of two samples with different process parameters, each subjected to varying  
82 parameters including scanning speed, laser power, as well as overlap percentage. A flow rate of 15 L/min of pure argon  
83 was employed as a protective gas during the cladding process with a fixed working distance at 358 mm of laser  
84 distance between the laser tip and the substrate for single-layer, single-pass cladding. The experiments were carried  
85 out to obtain a laser-clad layer that is nearly or completely free of cracks. Table 1 lists the LC parameters wherein the  
86 range of the laser power was restricted to 250–300 W in addition to the scanning velocity within 50–70 mm/s. With  
87 the two optimized process laser parameters, at the substrate interface, consistent coatings with strong metallurgical  
88 bonding may be achieved. All samples were sliced in the direction of the laser scanning once the cladding was finished.  
89 Every specimen's surface was mechanically polished to a mirror-like finish.

**Table 1:** The experimental parameters of LC

<b>Samples No.</b>	<b>Laser wavelength (nm)</b>	<b>Shielding gas flow (Ar) (l/min)</b>	<b>Laser power (W)</b>	<b>Scanning speed (mm/s)</b>	<b>Overlapping percentage (%)</b>
<b>1</b>	1070	15	280	50	30
<b>2</b>	1070	15	300	70	50

91 The preparation of metallography of fabricated samples for cross-sectional analysis involved polishing with  
 92 sandpaper and diamond powder until a mirror-like surface and scratch-free was obtained. Then, followed by chemical  
 93 etching of Linsenätzmittel solution (70 mL HCl, 1000 mL ethanol, 40 g FeCl<sub>3</sub>, as well as 30 g CuCl<sub>2</sub>) for a duration  
 94 of 1 minute [16]. The microstructure within the coating layer (CL) was examined through SEM analysis. The  
 95 crystallinity of the coating was assessed using X-Raya Diffraction (XRD, Miniflex, Rigaku, Japan) with Cu radiation  
 96 (Cu K $\alpha$ ,  $\lambda = 0.1541$  nm). Amorphous materials exhibit a diffuse scattering pattern instead of distinct diffraction peaks  
 97 due to the absence of long-range atomic order. The crystalline size of each sample was calculated using Scherrer's  
 98 equation, where D as **equation 1** [17] represents the crystalline size, K is the shape factor,  $\lambda$  is the X-ray wavelength,  
 99  $\beta$  is the full width at half maximum (FWHM) in radians, and  $\theta$  is the Bragg angle. The quantification of amorphous  
 100 content performed using the constant background method as **equation 2** [18], [19] was analyzed with PDXL software.  
 101 Energy dispersive X-ray spectroscopy (EDS) in conjunction with scanning electron microscopy (SEM, Phenom XL  
 102 Desktop) was utilized to analyze the phase as well as microstructure of laser-clad Fe-based alloy coatings.  
 103 Additionally, a Vickers microhardness tester (HV-1000, FALCON450G2) was employed to determine the  
 104 microhardness regarding the cross-sections as well as post-processed coated surfaces. The tester was utilized with a  
 105 force of 10 kgf and a 10-second dwell period [5]. Microhardness was measured at three points on each CL surface,  
 106 and the average was calculated.

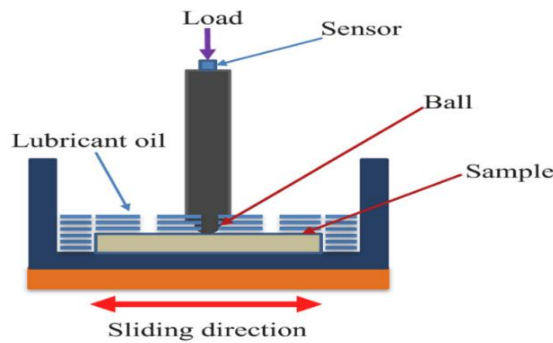
$$107 \quad D = \frac{K\lambda}{\beta \cos\theta} \quad (\text{Equation 1})$$

$$108 \quad \text{Amorphous content (AC)} = \frac{\text{Area under the amorphous background}}{\text{Area under the XRD pattern}} \quad (\text{Equation 2})$$

109

110 The FeCrMoCB amorphous coating's wear resistance was evaluated by means of dry and lubricated sliding  
 111 wear tests, which were carried out in ambient conditions via a high-frequency reciprocating rig tribometer (HFRR)  
 112 along with commercially available AISI 52100 steel balls with a 6 mm diameter as counterparts. Figure 2 depicts a

113 schematic of the wear test. Prior to testing, two coating samples underwent polishing to achieve a mirror finish,  
 114 ensuring uniform surface roughness across the specimens compared to uncoated polished steel. As stated in Table 2,  
 115 the wear tests were carried out in both lubricated as well as dry settings. Approximately 0.2 grams of mineral oil-based  
 116 automotive grease (NLGI 3) were applied to the samples as lubricants. NLGI 3 grease has a thicker consistency,  
 117 ensuring it stays in place and provides continuous lubrication even under high pressure and movement. This is  
 118 particularly important for automotive and industrial machinery. To minimize experimental error, three replicated wear  
 119 tests were conducted, and the average values of both the coefficient of friction (COF) as well as wear volume were  
 120 presented. As per ASTM G133-02, weight loss is a standard method for assessing wear loss [16], [20]. Hence, wear  
 121 volume loss was computed via the formula  $V_{loss} = (m_{before} - m_{after})/\rho$ , in which  $V_{loss}$  represents the wear volume  
 122 ( $\text{mm}^3$ ),  $m$  denotes the measured weight of the samples before and after wear, and  $\rho$  is the density of the substrate [5].  
 123 The wear scars on the sample surfaces after the dry as well as lubricated wear test were determined utilizing SEM.



124  
 125  
 126

**Figure 2:** Schematic of High-frequency reciprocating equipment

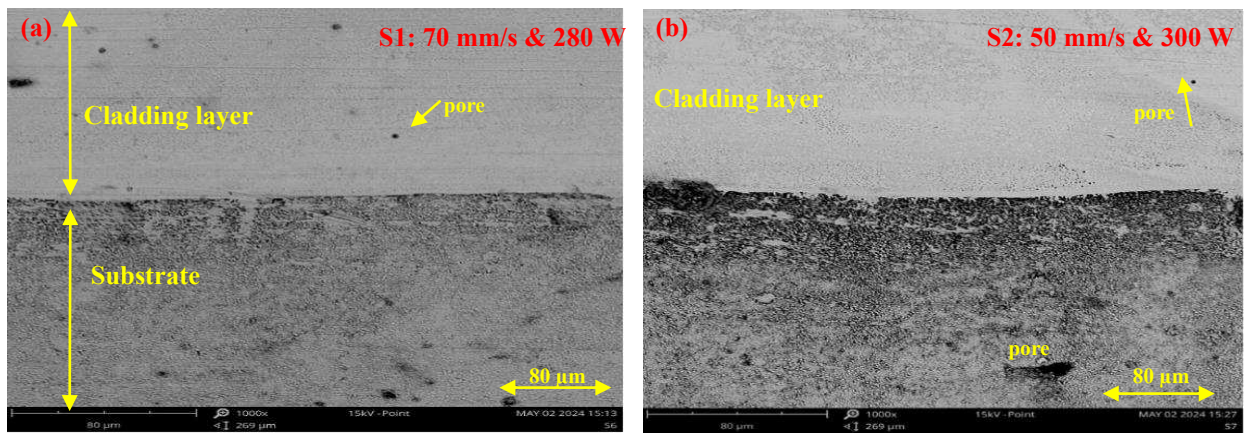
**Table 2:** Wear test conditions

Sliding condition	Dry	Lubricated
Load (N)	5	10
Sliding speed (m/s)	0.2	0.2
Room temperature (°c)	Room temp.	Room temp.
Sliding distance (m)	576	576
Stroke length (mm)	8	8
Friction time (minutes)	60	60

127 **3 Results and discussion**

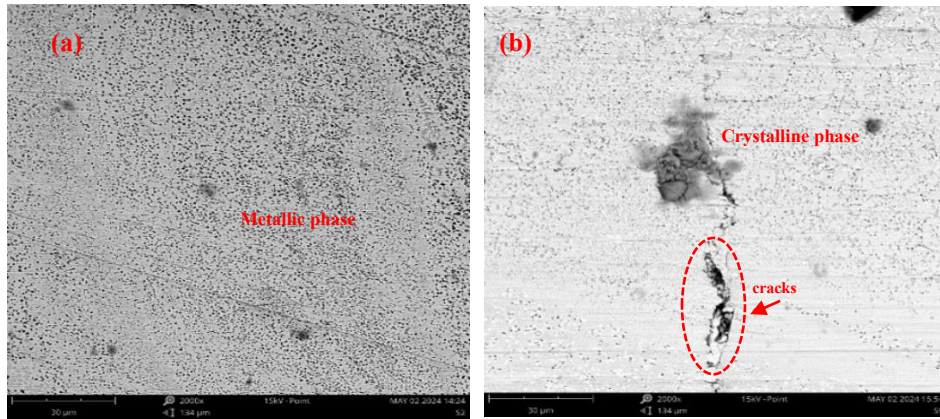
128 **3.1 Structural characterization of the coatings**

129 The cross-sectional morphology pertaining to the LC coating is shown in Figure 3, which shows that there are no gaps  
130 or cracks in any of the coatings because they are all completely merged with the substrate. Rapid heating causes some  
131 of the substrate surface to melt and forms a metallurgical link with the coating, resulting in a slightly curved border  
132 between the two materials [21]. On the surface of coating samples S1, there is a 50  $\mu\text{m}$ -diameter pore. This happens  
133 as a result of the molten pool's liquid flowing quickly and causing splashing, which causes small pores to grow during  
134 cladding. Several pores with sizes less than 5  $\mu\text{m}$  are seen on the surfaces of coatings S2, especially close to the  
135 coating/substrate interface where the greatest number of pores is found. This happens as a result of the molten pool's  
136 bottom gas being difficult to release during the LC process. Increasing the laser power enhances the coating/substrate  
137 contact and gets rid of gas pores when the scanning speed remains constant. On the other hand, insufficient laser power  
138 can also cause cracks and pores because of the existence of unmelted powder particles [22]. In contrast, high laser  
139 power might cause cracks owing to excessive thermal stress [23]. Moreover, the ratio of the amorphous phase ratio  
140 falls with an increasing amount of laser power.



141  
142 **Figure 3:** The cross-sectional morphology of the coatings. (a) coating S1 and (b) coating S2

143 To compare how various power levels affect the coating's microstructure, coatings S1 and S2 were selected for  
144 observation. Figure 4(a) reveals that coating S1 contains relatively few grains, indicating a greater amorphous content.  
145 When comparing Figures 4(b) and Figure 4(a) together, it is evident that coating S2 contains a significantly higher  
146 number of grains compared to coating S1. This indicates that increasing the laser power encourages the coating's  
147 crystallization as well as a better metallic phase. Higher laser power leads to greater heat accumulation, minimizing  
148 the cooling rate in the Heat Affected Zone (HAZ) as well as raising the coating's grain size [24].



149

150

**Figure 4:** The microstructure of the coatings. (a) coating S1 and (b) coating S2

151 An EDS line scan was performed to investigate the coating as well as the substrate's element distribution, as shown

152 in Figure 5. Since the findings for both coatings are identical, just the EDS line scan result for coating S1 is shown.

153 The coating area shows a uniform distribution of elements, with higher levels of Fe, Cr, and Mo. Past research indicates

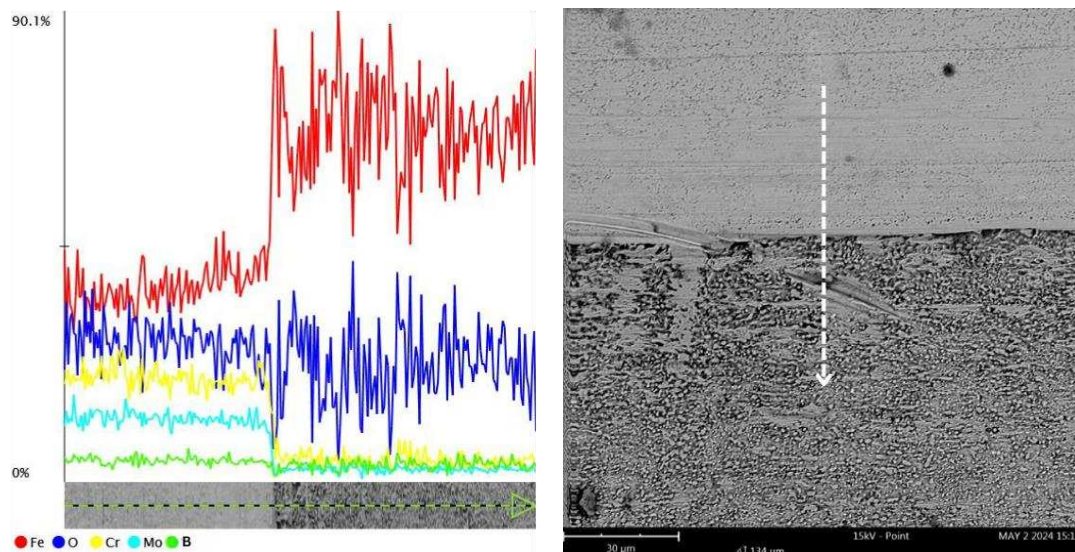
154 that adding trace amounts of Cr to amorphous alloys enables the formation of a protective surface film, effectively

155 preventing internal wear and corrosion [25]. Furthermore, by preventing Cr oxide from dissolving, Mo improves

156 pitting resistance while also maintaining the protective film and fostering chemical consistency [21]. The corrosion

157 resistance of the present Fe-based amorphous alloys is improved by Cr and Mo enrichment, making them ideal for

158 cost-effective, high-strength, and corrosion-resistant applications [26].



159

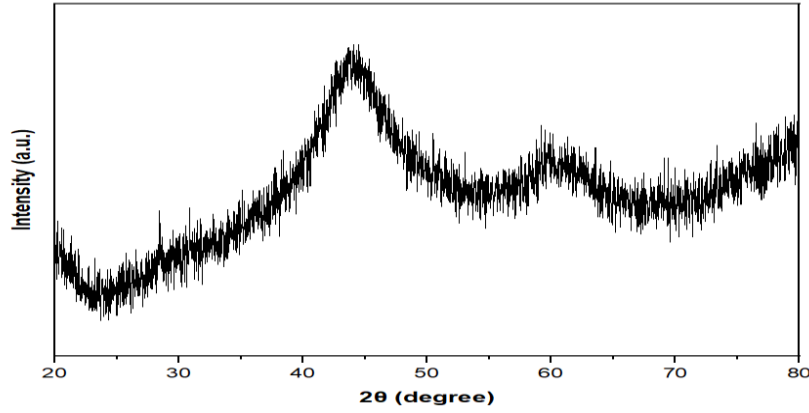
160

**Figure 5:** The EDS of the coating S1 and the line scan

### 161 3.2 Amorphous content

162 The Fe-based amorphous powder's XRD patterns are illustrated in Figure 6. The usual halo peaks at 40 to 47° confirm  
163 the powder's complete amorphous state, and there are other weak peaks representing crystalline phases. As a result,  
164 the powders consist mostly of amorphous phases with trace amounts of crystal phases. The XRD patterns for two  
165 samples of laser-clad coatings made at various process settings are shown in Figure 7, where the Full Width at Half  
166 Maximum (FWHM) of the XRD peaks is used to quantify grain size. The two coatings display five crystal phases of  
167 Fe, C, Fe<sub>23</sub>B<sub>6</sub> Fe-Cr, as well as Fe<sub>3</sub>C, and their diffraction peak positions are nearly identical. In the meantime, the  
168 amorphous content of the different amorphous coatings is demonstrated in Figure 8. **Table 3** shows the XRD analysis  
169 for samples S1 and S2, detailing the FWHM and crystalline sizes at each peak, calculated using Scherrer's equation  
170 as **equation 1**. From table 3, the average crystalline sizes are 6.34 nm for S1 and 6.27 nm for S2, indicating a subtle  
171 structural variation and also highlighting a slight difference in crystallite size that may reflect structural variation  
172 between the samples. FWHM analysis of XRD peaks, especially around 44.5° and 45°, shows that the sharper peaks  
173 in S2 indicate larger crystallites, while the broader peaks in S1 suggest smaller grains or higher residual stress, which  
174 correlates with the increased hardness in S2 due to enhanced crystallization at higher laser power.

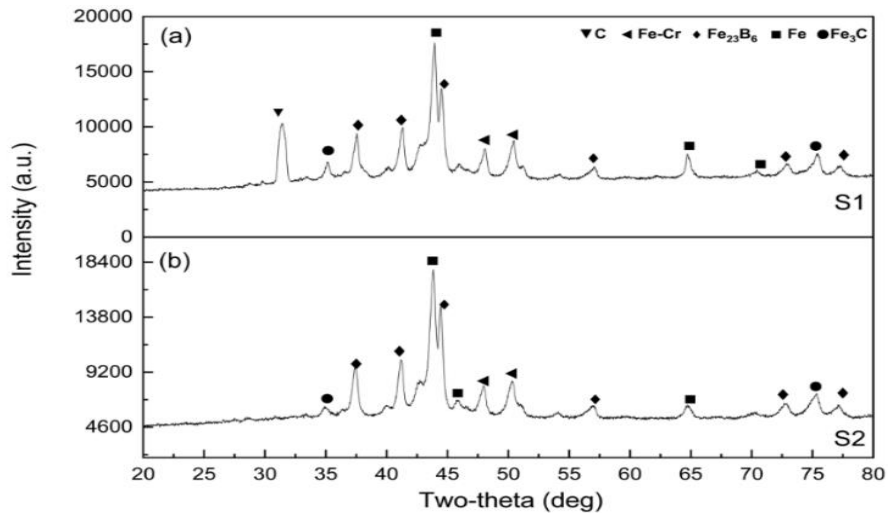
175 In the meantime, the amorphous content of the different amorphous coatings was estimated using the constant  
176 background method [27], [28] according to **equation 2** as result illustrated in Figure 8. The coatings S1 as well as S2  
177 possess a higher crystalline phase content, attributed to their maximum overlap of 50%. As adjacent passes overlap  
178 during cladding, the overlapping areas re-melt as well as re-solidify, having higher overlapping percentages causing  
179 thermal and residual stress that foster uniform grain nucleation and result in varied microstructures [29]. Since the  
180 underlying coating is not exposed to air and cannot cool instantly, it will undergo crystallization. Both samples show  
181 the presence of the same phases but with varying intensities. The relative peak heights suggest that coating S2 has  
182 more of the crystalline phases Fe<sub>23</sub>B<sub>6</sub> and Fe compared to S1 attributed to its use of the greatest laser power at 300  
183 W.



184

185

**Figure 6:** X-ray diffraction patterns of iron-based amorphous powder.



186

187

**Figure 7:** XRD patterns of Fe-based amorphous composite coatings: (a) S1 and (b) S2

188

**Table 3:** The full width at a half maximum (FWHM) and crystalline size of each peak position XRD signals from

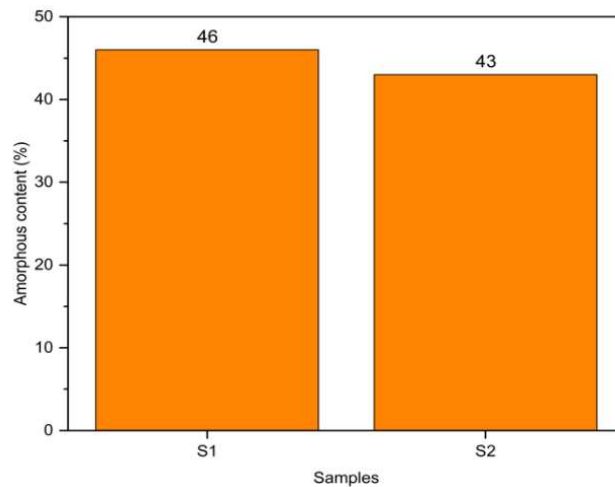
189

samples S1 and S2

Peak Position	S1			S2		
	2 $\theta$ ( $^{\circ}$ )	FWHM ( $\beta$ )	Crystalline Size, D (nm)	2 $\theta$ ( $^{\circ}$ )	FWHM ( $\beta$ )	Crystalline Size, D (nm)
1	31.40	0.79	10.33	34.92	7.85	1.06
2	35.10	3.56	2.33	37.46	0.76	10.89
3	37.56	0.84	9.92	41.18	0.80	10.55
4	41.32	0.89	9.51	43.84	0.75	11.34
5	43.94	0.69	12.26	44.44	0.51	16.72
6	44.52	0.55	15.59	45.82	1.68	5.13
7	48.10	1.46	5.95	47.96	1.39	6.21

8	50.46	1.76	4.96	50.3	1.71	5.10
9	57.04	8.82	1.02	56.94	8.24	1.09
10	64.70	2.85	3.29	64.72	5.12	1.83
11	70.40	5.00	1.94	72.66	5.30	1.85
12	72.86	2.00	4.93	75.34	2.42	4.14
13	75.40	2.64	3.80	60.5	1.61	5.69
14	82.06	3.66	2.87	81.9	1.71	6.13

190



191

192

**Figure 8:** Amorphous content of Fe-based amorphous composite coatings.

193

These two coating samples exhibit a balanced combination that comprises both crystalline and amorphous phases, providing a combination of wear resistance, hardness, toughness, as well as thermal stability. Thus, the higher level of amorphous content in S1 is reflected by its lower XRD peak intensities, whereas S2, with slightly lower amorphous content, shows higher peak intensities. This indicates that S2 possesses superior crystalline quality or a greater proportion of crystalline material compared to S1. Supported by literature [30], this balance is crucial for effective coatings, making samples S1 and S2 ideal for achieving optimal coating performance in industrial settings.

196

197

### 199 3.3 Microhardness

200

The fluctuation in microhardness over the clad specimen's thickness is depicted in Figure 9. Because of the synergistic strengthening effect from the amorphous phase, intermetallic compound, as well as solid solution, Fe-based amorphous coatings have microhardness 3 to 5 times greater than the substrate. Figure 9 depicts the cross-sectional microhardness distribution of the coated samples utilizing a step distance of 0.1 mm from the surface to a depth of 1.2 mm coating. Consequently, figure 9(i) the microhardness in S1 rapidly diminishes as we move from the coating layer

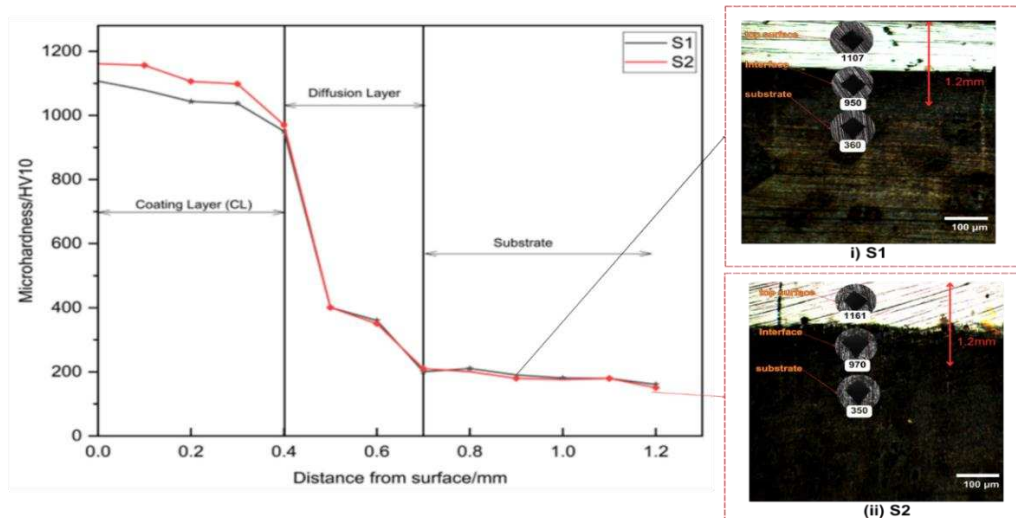
201

202

203

204

205 to the diffusion layer. For sample S1, the microhardness at the top surface reaches approximately 1107 HV10,  
 206 gradually decreasing to 950 HV10 at the interface, and further down to 360 HV10 in the substrate. This shows that S1  
 207 has a more gradual change in mechanical properties, which might result in stronger bonding between the coating and  
 208 the substrate. Meanwhile in figure 9(ii) samples S2 the top surface exhibits a slightly higher hardness of around 1161  
 209 HV10, transitioning to 970 HV10 at the interface, and reducing to 350 HV10 in the substrate, showing a similar  
 210 hardness it sharply decreases. This could improve durability and performance under mechanical stress. Samples S1  
 211 and S2 maintain the highest hardness values near the surface, with S2 showing a gradual decrease from 1161 HV10  
 212 at the surface to approximately 200 HV10 at 1.2 mm depth. This gradient is typical for hard coatings applied on softer  
 213 substrates, ensuring a hard, wear-resistant surface while preserving the overall toughness of the component [31]. This  
 214 is because the scanning speed, laser power, as well as overlapping percentage profoundly influence the surface  
 215 microhardness profiles of samples by determining the extent and uniformity of surface hardening. Thus, it generally  
 216 produces deeper and more consistent hardening, as demonstrated most effectively in both samples.



217  
 218 **Figure 9:** Microhardness profile along the cross-section of fabricated sample's different location: (i) S1 & (ii) S2

219 As shown in **Figure 7**, the variations in microhardness between samples S1 and S2 are closely linked to the distribution  
 220 of amorphous and crystalline phases. Regions exhibiting higher hardness correspond to areas with increased  
 221 crystalline content, where the dense atomic packing and limited dislocation enhance structural integrity. Conversely,  
 222 zones with a greater proportion of amorphous phases display lower hardness, as the disordered structure is more prone  
 223 to deformation. The data in **Figure 7** clearly reflect this relationship, providing a visual representation of how the

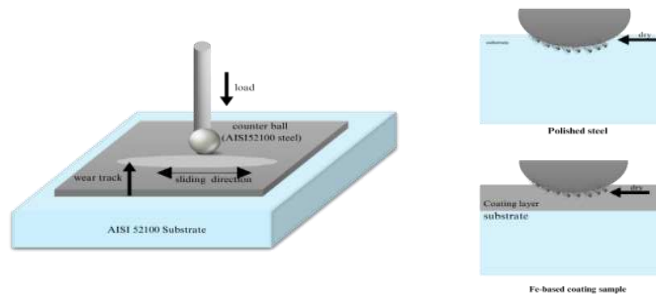
224 phase distribution affects hardness. This correlation not only clarifies the mechanisms behind hardness variations but  
225 also highlights the crucial role of phase composition in enhancing wear resistance and durability, key factors for the  
226 coating's performance in demanding applications. The microhardness of the FeCrMoCB coating is the highest; the  
227 cladding layer's average microhardness is approximately 1100 HV, 5 times greater than that of the AISI 52100 steel  
228 substrate [32]. This is about the same hardness as typical Fe-based amorphous composite coatings [29]. This high  
229 microhardness is attributed to the production of a greater fraction of amorphous phase in the coatings S1 as well as  
230 S2, as indicated by the results of XRD patterns and microstructures. Simultaneously, the incorporation of Cr into the  
231 composite coating has a strengthening impact on the supersaturated solid solution phenomena, which should be taken  
232 into account [33]. In the appropriate Fe-Cr ratio, the coating under study in this research displays a dense atomic  
233 accumulation condition. The coating is ideal for increasing the wear resistance of conventional industrial materials  
234 because of its high microhardness as well as elastic modulus, which outperform those of common steel and alloy.  
235 Overall, a higher overlapping percentage results in a thicker coating but with reduced microhardness. While the  
236 coating's diffusion zone is widened by greater laser power, the coating's microhardness is unaffected. As a result, the  
237 hard phase as well as the amorphous component have a direct impact on the coating's microhardness. Significant  
238 details about the coatings' structural integrity and wear resistance are provided by this analysis, which is essential for  
239 their application in high-stress environments.

## 240 **3.4 Friction and wear properties**

### 241 **3.4.1 Dry condition**

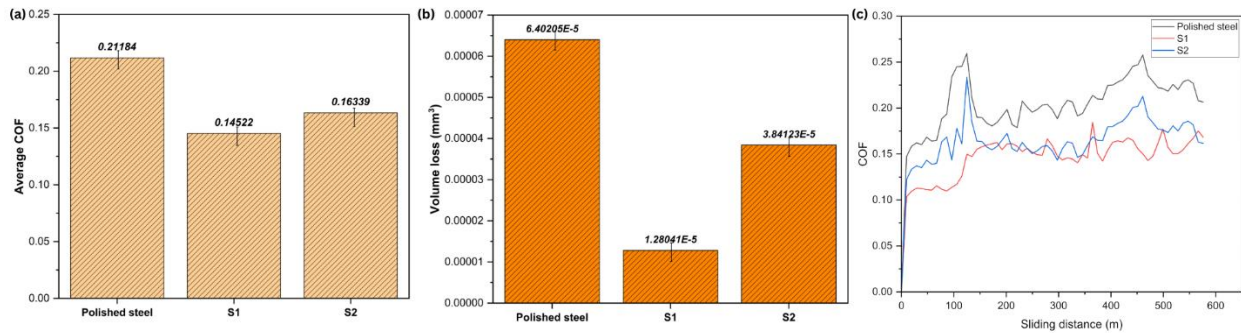
242 The main objective as well as prospective implementation of Fe-based amorphous composite coating, is to improve  
243 the wear resistance of metal substrates as a surface modification material. Both coated and uncoated systems were  
244 evaluated under identical conditions using an HFRR wear device with a fixed-ball configuration [26]. Dry sliding tests  
245 were conducted to assess the wear performance of the coatings in the absence of lubrication. This method is essential  
246 for evaluating how coatings behave under extreme wear conditions, as highlighted in previous studies. Khan H et al.  
247 (2024) emphasized that such tests can reveal important wear mechanisms, particularly in high-temperature and  
248 abrasive environments [34]. Additionally, Raushan et al. (2023) pointed out that these tests are useful in understanding  
249 how coatings resist friction and maintain adhesion under severe wear scenario [35]. Based on this, dry sliding tests  
250 were selected to simulate challenging real-world conditions for the FeCrMoCB coating. Figure 10 shows the schematic  
251 diagram experimental setup on dry condition. Figure 11 depicts the findings pertaining to dry sliding friction as well

252 as wear tests conducted on polished steel, as well as the coated samples S1 and S2. Figure 11(a) demonstrates that the  
 253 composite coatings S1 as well as S2 have average friction coefficients between 0.14 and 0.16. This suggests that the  
 254 coatings samples wear uniformly during the friction process in dry conditions and have good consistency in their  
 255 macrostructure. Combining Figures 11(b) as well as 11(c), it is evident that S1 exhibits the least volume loss  
 256 ( $0.0000128 \text{ mm}^3$ ) and consistently lower COF compared to S2, indicating superior wear resistance and stability under  
 257 dry sliding conditions. As observed in Figure 11(c), at the running-in stage, every curve quickly rose to a specific  
 258 value. Then, when the sliding distance rose (from 0-576 m), the friction changed into a rather steady wear stage  
 259 because of increased surface roughness as well as the tribo-layer's lubricating action. An elevated COF implies greater  
 260 difficulty for the wear ball to move around, hence raising the probability of adhesive wear [36]. The surface roughness  
 261 measurements for both samples, S1 and S2, were conducted before and after the wear tests under dry conditions using  
 262 the **3D Alicona InfiniteFocus** equipment. The initial surface roughness of S1 was found to be lower than that of S2  
 263 refer **table 4**, which had a significant impact on their tribological behavior. After wear testing in dry condition, both  
 264 samples exhibited increased roughness, with S2 experiencing a more substantial increase, further worsening its wear  
 265 performance. The COF, nevertheless, does not accurately represent wear resistance.



266  
267

**Figure 10:** Schematic presentation wear geometry HFRR setup on dry conditions



268  
269  
270

**Figure 11:** Tribological results for the polished steel, S6 and S7 samples under dry sliding conditions: (a) Average COF; (b) wear volume loss; (c) the change of COF with sliding distance for the coatings.

271 **Table 4:** Surface roughness measurement before and after tribological testing in dry conditions

272

273

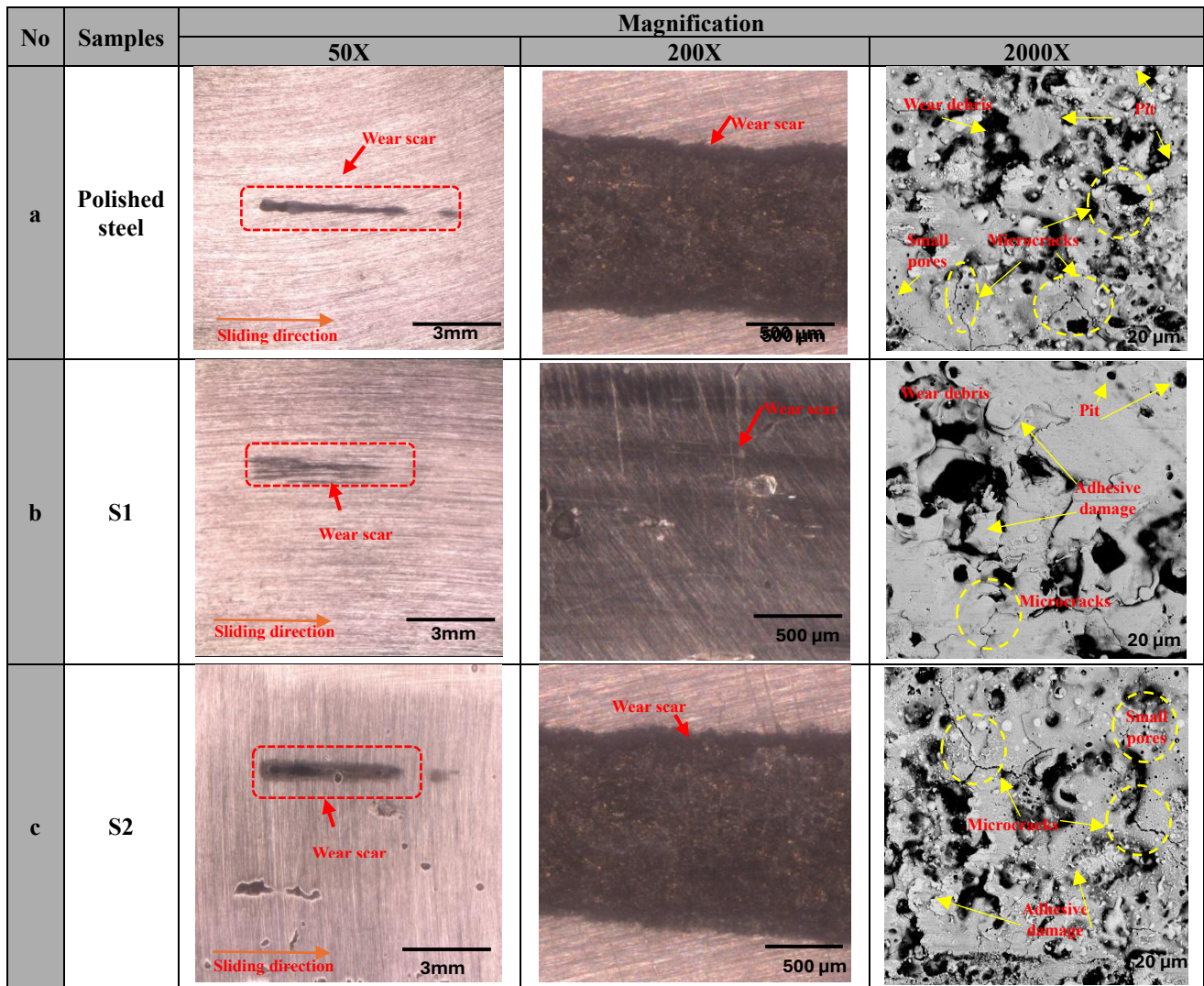
274

275

276

277

Samples	Roughness measurement, Ra ( $\mu\text{m}$ )	
	Before	After
Polished steel	0.137	0.353
S1	0.112	0.217
S2	0.124	0.237



278 **Figure 12:** SEM images of the wear tracks by dry conditions with three different magnifications: (a) polished steel;  
 279 (b) S1; (c) S2

280 Measuring the actual wear volume is necessary for a complete assessment. Generally, by lessening extreme plastic  
 281 deformation as well as preventing the spread of cracks, raising the hardness of steel can improve wear resistance[37].

282 Nonetheless, there is a complicated relationship between wear resistance as well as hardness. SEM images of wear  
 283 tracks under dry conditions shown in Figure 12 reveal that Sample S1 has the least surface damage, with minimal  
 284 grooves and smoother abrasive wear tracks, compared to S2 and polished steel, which display deeper grooves and  
 285 more severe wear features. The underlying layer of the hardness specimens had several tiny microcracks, as seen in  
 286 Figures 12(b) as well as 12(c). Since spherical carbides are a hard secondary phase, they tend to produce local stress  
 287 concentrations as well as facilitate crack initiation, as seen by the tendency of microcracks to form around them [37].

288 As discussed above, Figure 13 illustrates the failure wear mechanisms on dry sliding friction of all specimens. Polished  
 289 steel shows the greatest wear scar depth, indicating less wear resistance than samples S1 and S2, which exhibit better  
 290 wear resistance despite microcracks, particularly in S2, due to pre-existing flaws. The AISI 52100 steel's surface layer  
 291 nanocrystal production reinforces the martensite matrix and prevents the spread of microcracks [38]. However, the  
 292 current wear test results show that the amorphous content as well as the crystalline phase composition, impact wear  
 293 resistance, and mechanisms during dry sliding under given loads. Thus, the S1 specimen demonstrated the best wear  
 294 performance.

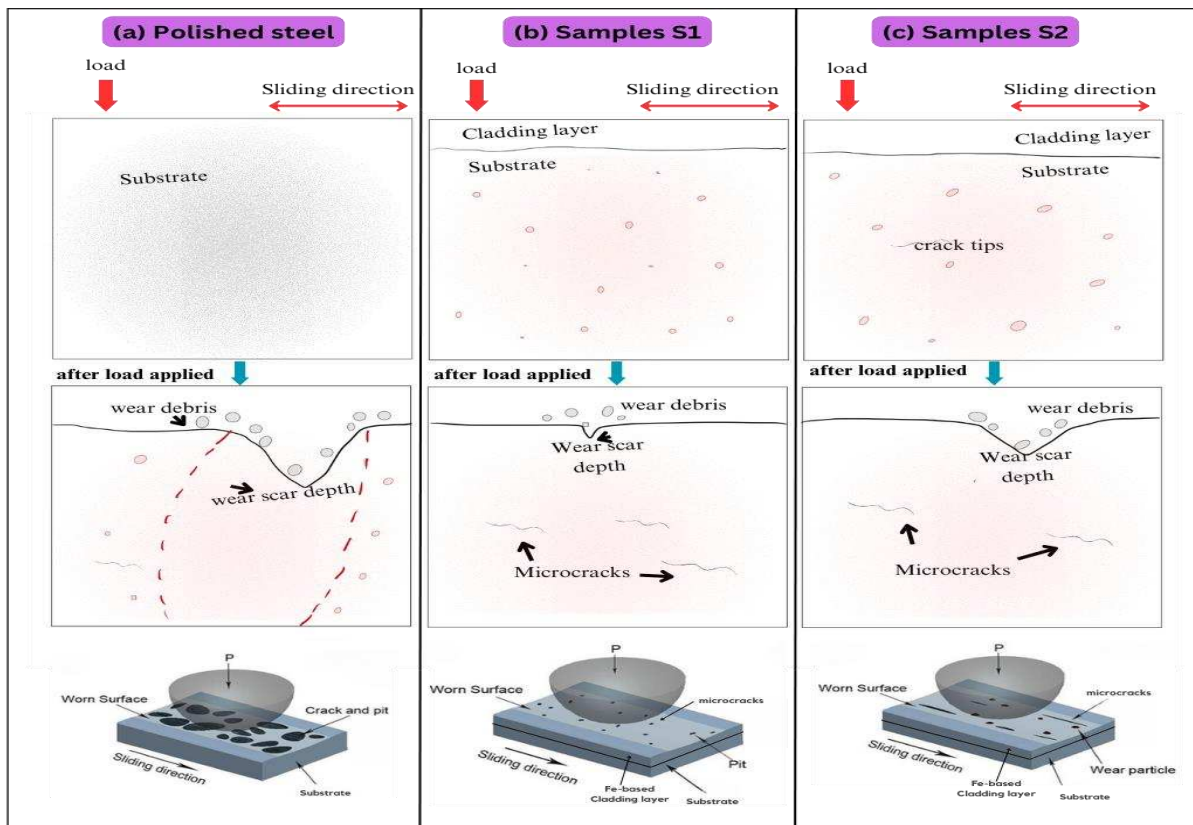
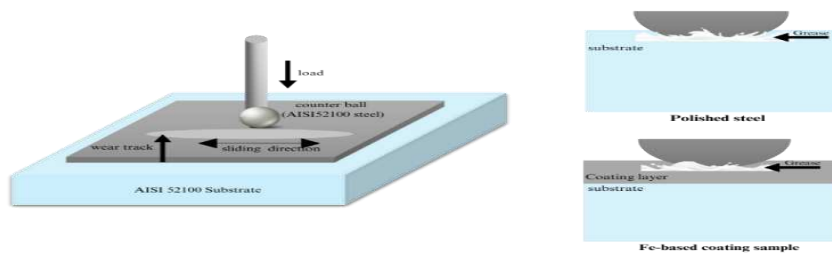


**Figure 13:** Schematics of wear mechanism during sliding dry condition: (a) polished steel; (b) S1 and (c) S2

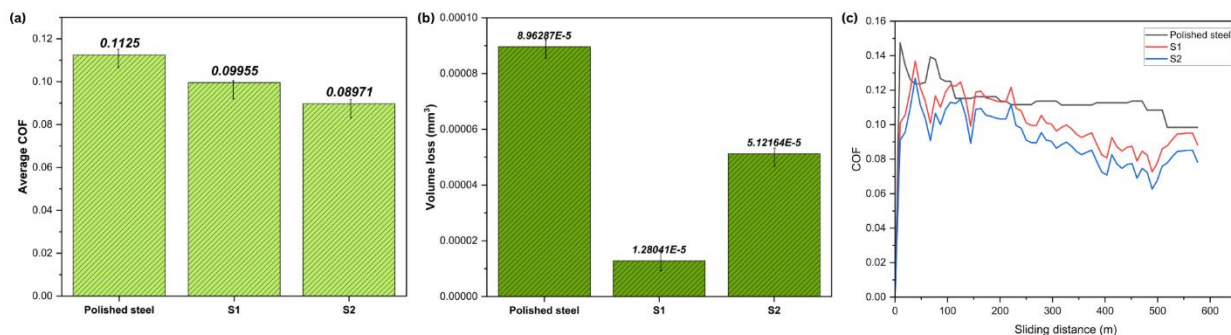
295  
296

297 **3.4.2 Lubricated condition**

298 Grease is used in HFRR testing to simulate actual operating conditions where grease is used as a lubricant.  
 299 Approximately 0.2 g of grease was evenly spread on the samples to ensure consistent coverage and reliable results.  
 300 Figure 14 shows the schematic diagram experimental setup on grease-lubricated condition. When the conditions are  
 301 properly lubricated, Figure 15 shows how the wear volume and average COF during the stable stage vary with  
 302 amorphous content. Figures 15(a) and 15(b) show that **S1 and S2** exhibit lower average COF values (0.09955 and  
 303 0.08971, respectively) compared to polished steel (0.1125). This reduction indicates that S1 and S2 have superior  
 304 frictional properties, leading to less resistance during sliding. In the friction pair, a higher COF means the wear ball  
 305 has more difficulty sliding, making adhesive wear more likely to occur [39]. Meanwhile, Figure 15(c) illustrates that  
 306 over the sliding distance, **S1 and S2** maintain lower COF values compared to polished steel. Combining these  
 307 observations, Sample S1 stands out as the most effective in reducing friction and resisting wear under grease-lubricated  
 308 conditions, followed by Sample S2, which also surpasses polished steel in performance. In the **grease-lubricated**  
 309 **condition**, the lubrication layer reduced direct contact between asperities, which made the impact of surface roughness  
 310 less significant as result shown in **table 5**. Despite this, S1 still demonstrated better wear resistance due to its initially  
 311 smoother surface, while S2 continued to exhibit higher COF and wear volume, though to a lesser extent than in the  
 312 lubricated condition.



313 **Figure 14:** Schematic presentation wear geometry HFRR setup on grease-lubricated conditions

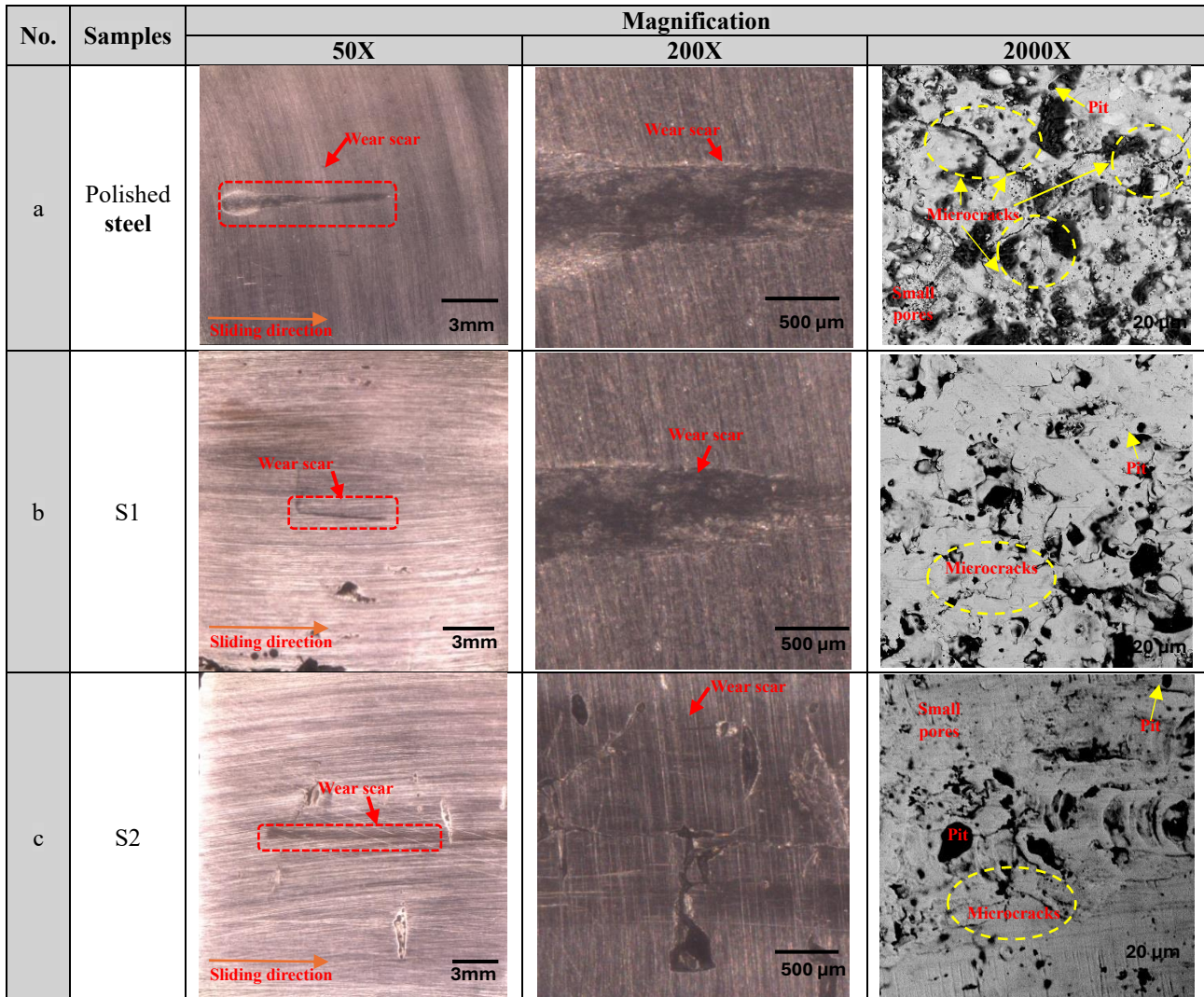


314 **Figure 15:** Tribological results for the polished steel, S1 and S2 samples under lubricated sliding conditions: (a)  
 315 Average COF; (b) wear volume loss; (c) the change of COF with sliding distance for the coatings.

319  
 320  
 321  
 322  
 323  
 324  
 325  
 326

**Table 5:** Surface roughness measurement before and after tribological testing in lubricated conditions

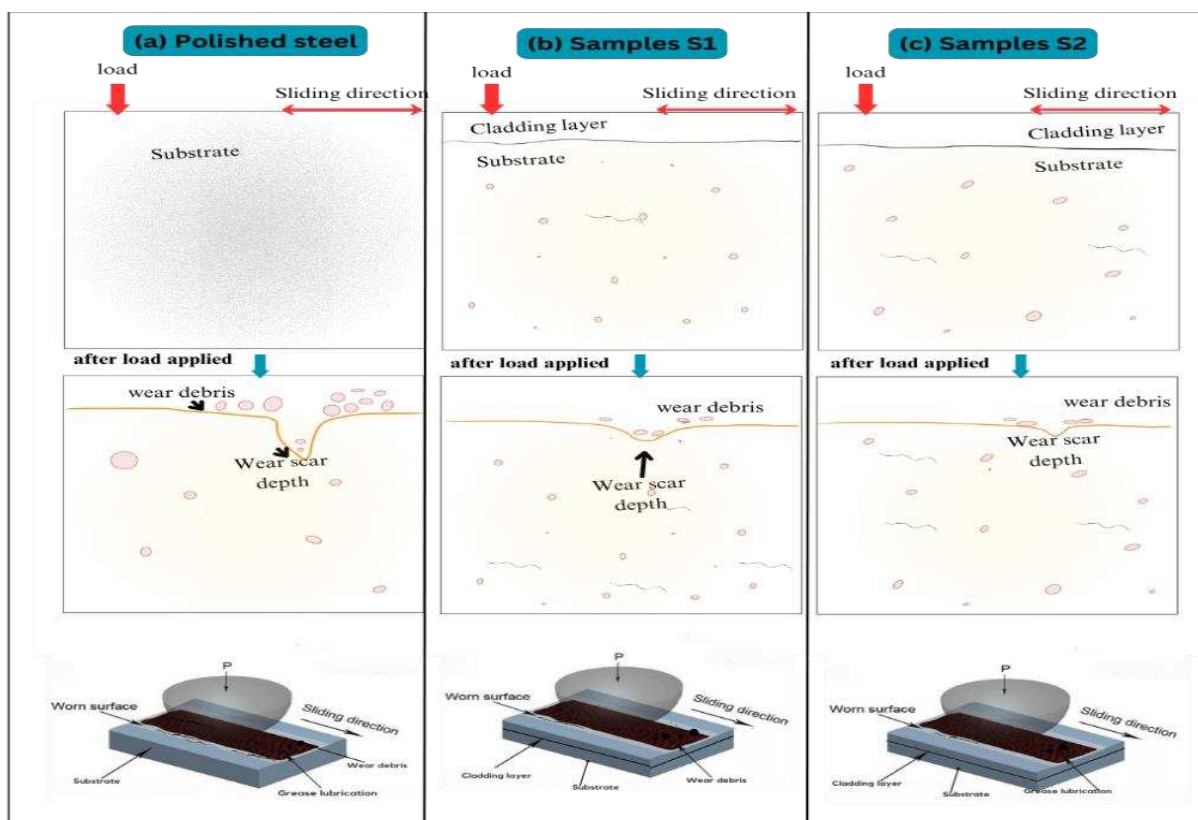
Samples	Roughness measurement, Ra ( $\mu\text{m}$ )	
	Before	After
Polished steel	0.137	0.201
S1	0.111	0.136
S2	0.118	0.151



327 **Figure 16:** SEM images of the wear tracks by lubricated conditions three different magnifications: (a) polished  
 328 steel; (b) S1 and (c) S2

329 The wear tests were conducted with adequate lubrication, but a higher frictional load than usual was applied to observe  
 330 the worn morphology, as shown in Figure 16. In summary, the comparative analysis of these three figures reveals that  
 331 S1 and S2 both exhibit superior wear resistance and lower friction under lubricated conditions compared to polished

332 steel. For every sample, straight wear signs denote abrasion wear, and rough marks represent adhesion wear. The  
 333 brittle-ductile-brittle mode is how wear debris is removed, commonly observed in metallic glasses (MGs) [40]. Where,  
 334 sample S1 stands out with the lowest average COF, minimal wear volume loss, and the most stable COF during sliding.  
 335 Figure 17 illustrates the failure wear mechanisms on grease-lubricated sliding friction of all specimens. The S2  
 336 samples exhibit the least wear scar depth, indicating superior wear resistance compared to S1 and polished steel. To  
 337 minimize wear volume and enhance wear resistance, it is beneficial to avoid excessive hardness as well as enhance  
 338 the spherical carbides' contents. Pertaining to AISI 52100 bearing steel, the main failure wear modes observed are  
 339 abrasive wear and fatigue wear [38]. The outcomes of the wear test demonstrate the improved wear resistance of the  
 340 FeCrMoCB metallic glass (MG) composite in both dry as well as grease-lubricated conditions.



341  
 342 **Figure 17:** Schematics of wear mechanism during sliding lubricated condition: (a) polished steel; (b) S1 and (c) S2  
 343

344 In this study shows that the FeCrMoCB coating significantly improves microhardness and wear resistance, with  
 345 Sample S1 reducing wear volume by 95% under dry conditions. This is attributed to its higher amorphous content,  
 346 which enhances crack resistance, while Sample S2's higher crystalline content improves toughness. Similar studies  
 347 confirm that coatings with higher amorphous content exhibit superior wear performance, as seen in Pan et al. [41], who

348 achieved 1280 HV0.1 hardness, and Si et al. [42], who reported 90.23% amorphous content leading to improved wear  
349 resistance. These findings reinforce the importance of phase balance in optimizing hardness and durability, making  
350 these coatings ideal for industrial applications requiring long-term mechanical stability.

#### 351 **4 Conclusion**

352 In this particular work, LC effectively developed a new Fe-based amorphous composite coating on an AISI 52100  
353 steel substrate. Through the formation of hardening phases such as Mo and Cr compounds and the reduction of  
354 crystalline phase size, the research discovered sample S1 that boosting the laser power to 280 W and scanning speed  
355 to 50 mm/s improves the amorphous content in the Fe-based cladding layer, hence boosting its hardness as well as  
356 wear resistance. Under a load of 10 kgf and 1000 HV, the FeCrMoCB amorphous composite coatings demonstrated  
357 good wear resistance as well as exceptional microhardness. The coating's amorphous nature gives it a high hardness  
358 as well as elastic modulus, which can drastically change the wear process and improve wear resistance. The amorphous  
359 content had no discernible effect on the wear volume or the average COF values at the stable stage in either lubricated  
360 or dry conditions. The combined impacts of the amorphous content, phase composition, as well as the size and  
361 distribution of the crystalline phase led to the different morphologies on the wear tracks and the change in the wear  
362 mechanism. These findings have promising industrial applications, particularly in sectors requiring enhanced wear  
363 performance, such as automotive and aerospace. Future research should focus on optimizing the coating composition  
364 for specific working conditions, such as extreme temperatures or high-load applications, to further improve its  
365 durability. Investigating additional modifications to the coating, such as nanostructuring or adding reinforcement  
366 phases, could offer further improvements in performance, making this technology even more attractive for practical  
367 industrial applications.

#### 368 **5 Credit authorship contribution statement**

369 **Mohamad Firdaus Saharudin**: Conceptualization, Methodology, Software, Investigation, Formal analysis, Writing  
370 – original draft. **N.W.M. Zulkifli & Mahmoud Z. Ibrahim**: Validation, Writing – review & editing, Supervision,  
371 Data curation and formal analysis. **Y. Goh, A. Morina & R. Mehtab**: Writing – review & editing, Formal analysis  
372 and supervision.

373 **6 Acknowledgements**

374 LiquidMetal@Coatings provided the Fe-based amorphous powder needed for this work, which the authors are grateful  
375 for. There was no specific grant awarded for this research by public, commercial, or nonprofit funding organizations.

376 **7 Declaration of Competing Interest**

377 The authors state that none of their known financial conflicts or interpersonal connections could have influenced the  
378 work that was published in this paper.

379 **8 Declaration of Generative AI and AI-assisted technologies in the writing process**

380 In order to paraphrase as well as modify sentence structures while keeping the original meaning, the authors employed  
381 Quillbolt AI during the development of this work. Following their use of this tool/service, the authors took full  
382 responsibility for the publication's content and reviewed and amended it as necessary.

383 **9 References**

- 384 [1] G.-S. Ham, K.-W. Kim, G.-S. Cho, C. P. Kim, and K.-A. Lee, "Fabrication, microstructure and wear properties  
385 of novel Fe-Mo-Cr-C-B metallic glass coating layers manufactured by various thermal spray processes,"  
386 *Mater Des*, vol. 195, p. 109043, Oct. 2020, doi: <https://10.1016/j.matdes.2020.109043>.
- 387 [2] S. L. Wang, Z. Y. Zhang, Y. B. Gong, and G. M. Nie, "Microstructures and corrosion resistance of Fe-based  
388 amorphous/nanocrystalline coating fabricated by laser cladding," *J Alloys Compd*, vol. 728, pp. 1116–1123,  
389 Dec. 2017, doi: <https://10.1016/j.jallcom.2017.08.251>.
- 390 [3] G. Y. Koga *et al.*, "Challenges in optimizing the resistance to corrosion and wear of amorphous Fe-Cr-Nb-B  
391 alloy containing crystalline phases," *J Non Cryst Solids*, vol. 555, p. 120537, Mar. 2021, doi:  
392 <https://10.1016/j.jnoncrysol.2020.120537>.
- 393 [4] L. Wang, J. Wang, and M. Sun, "Mechanical properties of Fe-based bulk amorphous  
394 Fe<sub>41</sub>Co<sub>7</sub>Cr<sub>15</sub>Mo<sub>14</sub>C<sub>15</sub>B<sub>6</sub>Y<sub>2</sub> alloy rods," *Chem Phys Lett*, vol. 750, p. 137511, Jul. 2020, doi:  
395 <https://10.1016/j.cplett.2020.137511>.
- 396 [5] C. Li, J. Zhai, L. Tian, Y. Lu, X. Li, and S. Kou, "Fabrication of Fe-based amorphous composite coating by  
397 laser cladding," *J Non Cryst Solids*, vol. 589, Aug. 2022, doi: <https://10.1016/j.jnoncrysol.2022.121648>.
- 398 [6] H. Wang, Y. Cheng, X. Zhang, J. Yang, and C. Cao, "Effect of laser scanning speed on microstructure and  
399 properties of Fe based amorphous/ nanocrystalline cladding coatings," *Mater Chem Phys*, vol. 250, p. 123091,  
400 Aug. 2020, doi: <https://10.1016/j.matchemphys.2020.123091>.
- 401 [7] Y. Lu, G. Huang, Y. Wang, H. Li, Z. Qin, and X. Lu, "Crack-free Fe-based amorphous coating synthesized by  
402 laser cladding," *Mater Lett*, vol. 210, pp. 46–50, Jan. 2018, doi: <https://10.1016/j.matlet.2017.08.125>.
- 403 [8] M. M. Quazi, M. A. Fazal, A. S. M. A. Haseeb, F. Yusof, H. H. Masjuki, and A. Arslan, "Effect of rare earth  
404 elements and their oxides on tribo-mechanical performance of laser claddings: A review," *Journal of Rare*  
405 *Earths*, vol. 34, no. 6, pp. 549–564, Jun. 2016, doi: [https://10.1016/S1002-0721\(16\)60061-3](https://10.1016/S1002-0721(16)60061-3).

- 406 [9] P. Gargarella *et al.*, “Formation of Fe-based glassy matrix composite coatings by laser processing,” *Surf Coat*  
407 *Technol*, vol. 240, pp. 336–343, Feb. 2014, doi: <https://10.1016/j.surfcoat.2013.12.049>.
- 408 [10] H. Wang, Y. Cheng, X. Zhang, J. Yang, and C. Cao, “Effect of laser scanning speed on microstructure and  
409 properties of Fe based amorphous/ nanocrystalline cladding coatings,” *Mater Chem Phys*, vol. 250, p. 123091,  
410 Aug. 2020, doi: <https://10.1016/j.matchemphys.2020.123091>.
- 411 [11] Y. Zhu, Z. Li, J. Huang, M. Li, R. Li, and Y. Wu, “Amorphous structure evolution of high power diode laser  
412 cladded Fe–Co–B–Si–Nb coatings,” *Appl Surf Sci*, vol. 261, pp. 896–901, Nov. 2012, doi:  
413 <https://10.1016/j.apsusc.2012.08.120>.
- 414 [12] S. L. Wang, Z. Y. Zhang, Y. B. Gong, and G. M. Nie, “Microstructures and corrosion resistance of Fe-based  
415 amorphous/nanocrystalline coating fabricated by laser cladding,” *J Alloys Compd*, vol. 728, pp. 1116–1123,  
416 Dec. 2017, doi: <https://10.1016/j.jallcom.2017.08.251>.
- 417 [13] Y. Kang, Y. Chen, Y. Wen, B. Wu, and M. Song, “Effects of structural relaxation and crystallization on the  
418 corrosion resistance of an Fe-based amorphous coating,” *J Non Cryst Solids*, vol. 550, p. 120378, Dec. 2020,  
419 doi: <https://10.1016/j.jnoncrysol.2020.120378>.
- 420 [14] S. Zhou *et al.*, “Effect of laser remelting on microstructure and properties of WC reinforced Fe-based  
421 amorphous composite coatings by laser cladding,” *Opt Laser Technol*, vol. 103, pp. 8–16, Jul. 2018, doi:  
422 <https://10.1016/j.optlastec.2018.01.024>.
- 423 [15] M. Z. Ibrahim, A. A. D. Sarhan, T. Y. Kuo, F. Yusuf, M. Hamdi, and C. S. Chien, “Investigate the effects of  
424 the substrate surface roughness on the geometry, phase transformation, and hardness of laser-cladded Fe-based  
425 metallic glass coating,” *The International Journal of Advanced Manufacturing Technology*, vol. 98, no. 5–8,  
426 pp. 1977–1987, Sep. 2018, doi: <https://10.1007/s00170-018-2354-6>.
- 427 [16] M. Z. Ibrahim, A. A. D. Sarhan, T. Y. Kuo, F. Yusof, M. Hamdi, and T. M. Lee, “Developing a new laser  
428 cladded FeCrMoCB metallic glass layer on nickel-free stainless-steel as a potential superior wear-resistant  
429 coating for joint replacement implants,” *Surf Coat Technol*, vol. 392, Jun. 2020, doi:  
430 <https://10.1016/j.surfcoat.2020.125755>.
- 431 [17] T. Zeeshan, S. Anjum, H. Iqbal, and R. Zia, “Substitutional effect of copper on the cation distribution in cobalt  
432 chromium ferrites and their structural and magnetic properties,” *Materials Science- Poland*, vol. 36, no. 2, pp.  
433 255–263, 2018, doi: <https://10.1515/msp-2018-0011>.
- 434 [18] M. Z. Ibrahim, A. A. D. Sarhan, T. Y. Kuo, F. Yusof, and M. Hamdi, “Characterization and hardness  
435 enhancement of amorphous Fe-based metallic glass laser cladded on nickel-free stainless steel for biomedical  
436 implant application,” *Mater Chem Phys*, vol. 235, p. 121745, Sep. 2019, doi:  
437 <https://10.1016/j.matchemphys.2019.121745>.
- 438 [19] B. Manne, S. Bontha, M. R. Ramesh, M. Krishna, and V. K. Balla, “Solid state amorphization of Mg-Zn-Ca  
439 system via mechanical alloying and characterization,” *Advanced Powder Technology*, vol. 28, no. 1, pp. 223–  
440 229, Jan. 2017, doi: <https://10.1016/j.apt.2016.09.032>.

- 441 [20] H. Zhang, Y. Hu, G. Hou, Y. An, and G. Liu, "The effect of high-velocity oxy-fuel spraying parameters on  
442 microstructure, corrosion and wear resistance of Fe-based metallic glass coatings," *J Non Cryst Solids*, vol.  
443 406, pp. 37–44, Dec. 2014, doi: <https://10.1016/j.jnoncrsol.2014.09.041>.
- 444 [21] C. Li, J. Zhai, L. Tian, Y. Lu, X. Li, and S. Kou, "Fabrication of Fe-based amorphous composite coating by  
445 laser cladding," *J Non Cryst Solids*, vol. 589, Aug. 2022, doi: <https://10.1016/j.jnoncrsol.2022.121648>.
- 446 [22] P. Zhang, J. Tan, Y. Tian, H. Yan, and Z. Yu, "Research progress on selective laser melting (SLM) of bulk  
447 metallic glasses (BMGs): a review," *The International Journal of Advanced Manufacturing Technology*, vol.  
448 118, no. 7–8, pp. 2017–2057, Feb. 2022, doi: <https://10.1007/s00170-021-07990-8>.
- 449 [23] H. X. Li, Z. C. Lu, S. L. Wang, Y. Wu, and Z. P. Lu, "Fe-based bulk metallic glasses: Glass formation,  
450 fabrication, properties and applications," *Prog Mater Sci*, vol. 103, pp. 235–318, Jun. 2019, doi:  
451 <https://10.1016/j.pmatsci.2019.01.003>.
- 452 [24] H. Wang, Y. Cheng, R. Geng, B. Wang, Y. Chen, and X. Liang, "Comparative study on microstructure and  
453 properties of Fe-based amorphous coatings prepared by conventional and high-speed laser cladding," *J Alloys  
454 Compd*, vol. 952, p. 169842, Aug. 2023, doi: <https://10.1016/j.jallcom.2023.169842>.
- 455 [25] H. Wang *et al.*, "Influence of scanning speed on microstructure and corrosion resistance of Fe-based  
456 amorphous coatings by high-speed laser cladding," *Surf Coat Technol*, vol. 479, p. 130449, Mar. 2024, doi:  
457 <https://10.1016/j.surfcoat.2024.130449>.
- 458 [26] H. Wang, Y. Cheng, R. Geng, B. Wang, Y. Chen, and X. Liang, "Comparative study on microstructure and  
459 properties of Fe-based amorphous coatings prepared by conventional and high-speed laser cladding," *J Alloys  
460 Compd*, vol. 952, p. 169842, Aug. 2023, doi: <https://10.1016/j.jallcom.2023.169842>.
- 461 [27] M. Z. Ibrahim, A. A. D. Sarhan, T. Y. Kuo, F. Yusof, and M. Hamdi, "Characterization and hardness  
462 enhancement of amorphous Fe-based metallic glass laser clad on nickel-free stainless steel for biomedical  
463 implant application," *Mater Chem Phys*, vol. 235, p. 121745, Sep. 2019, doi:  
464 <https://10.1016/j.matchemphys.2019.121745>.
- 465 [28] B. Manne, S. Bontha, M. R. Ramesh, M. Krishna, and V. K. Balla, "Solid state amorphization of Mg-Zn-Ca  
466 system via mechanical alloying and characterization," *Advanced Powder Technology*, vol. 28, no. 1, pp. 223–  
467 229, Jan. 2017, doi: <https://10.1016/j.apt.2016.09.032>.
- 468 [29] X. Hou, D. Du, K. Wang, Y. Hong, and B. Chang, "Microstructure and Wear Resistance of Fe-Cr-Mo-Co-C-  
469 B Amorphous Composite Coatings Synthesized by Laser Cladding," *Metals (Basel)*, vol. 8, no. 8, p. 622, Aug.  
470 2018, doi: <https://10.3390/met8080622>.
- 471 [30] M. Xiao *et al.*, "Microstructure and mechanical properties of Fe-based amorphous alloy coatings prepared by  
472 ultra-high speed laser cladding," *Mater Lett*, vol. 297, p. 130002, Aug. 2021, doi:  
473 <https://10.1016/j.matlet.2021.130002>.
- 474 [31] K. Li, J. Liang, and J. Zhou, "Preparation and characterization of laser clad FeCrMoBSi amorphous  
475 composite coatings," *Surf Coat Technol*, vol. 423, Oct. 2021, doi: <https://10.1016/j.surfcoat.2021.127520>.

- 476 [32] A. Panda, A. K. Sahoo, R. Kumar, and R. K. Das, “A review on machinability aspects for AISI 52100 bearing  
477 steel,” in *Materials Today: Proceedings*, Elsevier Ltd, 2020, pp. 617–621. doi:  
478 <https://10.1016/j.matpr.2019.05.422>.
- 479 [33] S. Zhou *et al.*, “Effect of laser remelting on microstructure and properties of WC reinforced Fe-based  
480 amorphous composite coatings by laser cladding,” *Opt Laser Technol*, vol. 103, pp. 8–16, Jul. 2018, doi:  
481 <https://10.1016/j.optlastec.2018.01.024>.
- 482 [34] H. Khan, J. S. Gill, A. Bansal, and V. Singh, “Slurry Abrasion and Dry Sliding Behavior of High-Velocity  
483 Oxy-Fuel (HVOF) Sprayed WC-12Co and WC-10Co-4Cr Coatings on EN8 Tillage Material,” *Journal of*  
484 *Thermal Spray Technology*, vol. 33, no. 5, pp. 1526–1543, Jun. 2024, doi: [https://10.1007/s11666-024-01779-](https://10.1007/s11666-024-01779-3)  
485 [3](https://10.1007/s11666-024-01779-3).
- 486 [35] H. Raushan *et al.*, “Dry sliding and slurry abrasion behaviour of wire arc additive manufacturing – Cold metal  
487 transfer (WAAM-CMT) clad in Inconel 625 on EN8 steel,” *Tribol Int*, vol. 179, p. 108176, Jan. 2023, doi:  
488 <https://10.1016/j.triboint.2022.108176>.
- 489 [36] J. B. Cheng, X. B. Liang, Z. H. Wang, and B. S. Xu, “Dry sliding friction and wear properties of metallic glass  
490 coating and martensite stainless coating,” *Tribol Int*, vol. 60, pp. 140–146, Apr. 2013, doi:  
491 <https://10.1016/j.triboint.2012.11.010>.
- 492 [37] Y. Li *et al.*, “Wear behavior and damage characterization for AISI 52100 bearing steels: Effect of hardness  
493 and spherical carbides,” *Journal of Materials Research and Technology*, vol. 30, pp. 8359–8370, May 2024,  
494 doi: <https://10.1016/j.jmrt.2024.05.220>.
- 495 [38] Y. Li *et al.*, “Wear behavior and damage characterization for AISI 52100 bearing steels: Effect of hardness  
496 and spherical carbides,” *Journal of Materials Research and Technology*, vol. 30, pp. 8359–8370, May 2024,  
497 doi: <https://10.1016/j.jmrt.2024.05.220>.
- 498 [39] C. Li, J. Zhai, L. Tian, Y. Lu, X. Li, and S. Kou, “Fabrication of Fe-based amorphous composite coating by  
499 laser cladding,” *J Non Cryst Solids*, vol. 589, Aug. 2022, doi: <https://10.1016/j.jnoncrystsol.2022.121648>.
- 500 [40] M. Z. Ibrahim, A. A. D. Sarhan, T. Y. Kuo, F. Yusof, M. Hamdi, and T. M. Lee, “Developing a new laser  
501 clad FeCrMoCB metallic glass layer on nickel-free stainless-steel as a potential superior wear-resistant  
502 coating for joint replacement implants,” *Surf Coat Technol*, vol. 392, Jun. 2020, doi:  
503 <https://10.1016/j.surfcoat.2020.125755>.
- 504 [41] C. Pan *et al.*, “Preparation of high performance Fe-based amorphous coating by resistance seam welding,”  
505 *Surf Coat Technol*, vol. 408, p. 126813, Feb. 2021, doi: <https://10.1016/j.surfcoat.2020.126813>.
- 506 [42] C. Si, B. Duan, Q. Zhang, J. Cai, and W. Wu, “Microstructure, corrosion-resistance, and wear-resistance  
507 properties of subsonic flame sprayed amorphous Fe–Mo–Cr–Co coating with extremely high amorphous  
508 rate,” *Journal of Materials Research and Technology*, vol. 9, no. 3, pp. 3292–3303, May 2020, doi:  
509 <https://10.1016/j.jmrt.2020.01.024>.
- 510